Ground Measurements for the Validation of Land Surface Temperatures Derived from AATSR and MODIS Data

César Coll, Vicente Caselles, Joan M. Galve, Enric Valor, Raquel Niclòs, Juan M. Sánchez and Raúl Rivas
Department of Thermodynamics, Faculty of Physics, University of Valencia.
50, Dr. Moliner. 46100 Burjassot, SPAIN.
Email: cesar.coll@uv.es

ABSTRACT

An experimental site was set up in a large, flat and homogeneous area of rice crops for the validation of satellite derived land surface temperature (LST). Experimental campaigns were held in the summers of 2002-04, when rice crops show full vegetation cover. LSTs were measured radiometrically along transects covering an area of 1 km^2. A total number of four thermal radiometers were used, which were calibrated and inter-compared through the campaigns. Radiometric temperatures were corrected for emissivity effects using field emissivity and downwelling sky radiance measurements. A database of ground-based LSTs corresponding to morning, cloud-free overpasses of Envisat/Advanced Along-Track Scanning Radiometer (AATSR) and Terra/Moderate Resolution Imaging Spectroradiometer (MODIS) is presented. Ground LSTs ranged from 25 to 32 ºC, with uncertainties between ±0.5 and ±0.9 ºC. The largest part of these uncertainties was due to the spatial variability of surface temperature. The database was used for the validation of LSTs derived from the operational AATSR and MODIS split-window algorithms, which are currently used to generate the LST product in the L2 level data. A quadratic, emissivity dependent split-window equation applicable to both AATSR and MODIS data was checked as well. Although the number of cases analyzed is limited (five concurrences for AATSR and eleven for MODIS), it can be concluded that the split-window algorithms work well, provided that the characteristics of the area are adequately prescribed, either through the classification of the land cover type and the vegetation cover, or with the surface emissivity. In this case, the AATSR LSTs yielded an average error or bias of -0.9 ºC (ground minus algorithm), with a standard deviation of 0.9 ºC. The MODIS LST product agreed well with the ground LSTs, with differences comparable or smaller than the uncertainties of the ground measurements for most of the days (bias of +0.1 ºC and standard deviation of 0.6 ºC, for cloud-free cases and viewing angles smaller than 60º). The quadratic split-window algorithm resulted in small average errors (+0.3 ºC for AATSR and 0.0 ºC for MODIS), with differences not exceeding ±1.0 ºC for most of the days (standard deviation of 0.9 ºC for AATSR and 0.5 ºC for MODIS).

1. INTRODUCTION

Land surface temperature (LST) is a very important parameter controlling the energy and water balance between the atmosphere and the land surface. Thermal infrared (TIR) remote sensing is the only possibility to retrieve LST over large portions of the Earth surface at different spatial resolutions and periodicities. However, the retrieval of LST from satellite data requires the correction for the effects introduced by the atmosphere, mainly the absorption and emission of atmospheric water vapor, and the surface emissivity, which can be significantly lower than unity and varies spatially with surface cover and type. Several approaches have been developed for the retrieval of LST from TIR data in the last 20 years (see Dash et al., 2002, for a revision). All these techniques need to be validated with ground measurements, what is rarely done because the difficulty of making ground measurements of LST comparable with satellite data. As recognized in Slater et al. (1996) and Wan et al. (2002), validation sites must be in areas larger than the pixel size with homogeneous cover both in terms of surface temperature and emissivity. It is required that the spatial variability of temperature and emissivity is very small within one satellite pixel, so that ground, point measurements could be compared with satellite, area-averaged measurements. In order to minimize the variability of surface temperature and emissivity, water bodies (such as lakes and reservoirs) are often used for the vicarious calibration of satellite TIR radiometers. However, we consider that operational LST algorithms should be validated in real land surfaces. For this end, fully vegetated surfaces and bare surfaces or deserts are the most suitable.

Few databases exist with ground measurements of LST for the validation of satellite products. An exception is the field measurements described in Prata (1994) for different sites in Australia, which were used for validating LSTs derived from the National Oceanic and Atmospheric Administration/Advanced Very High Resolution Radiometer (NOAA/AVHRR). Data collection has continued along the years, and currently the ground data are being used for the validation of the LST product (Prata, 2003) of the Advanced Along-Track Scanning Radiometer (AATSR) onboard the Envisat satellite (Llewellyn-Jones et al., 2001). Other smaller databases were used in Wan et al. (2002 and 2004) for the validation of Terra/Moderate Resolution Imaging Spectroradiometer (MODIS) derived LSTs. The present work is a contribution to the existing number of databases of ground-based LSTs suitable for the validation of satellite-derived LSTs. To this end, an experimental site was established in a large (~100 km^2) agricultural area of rice crops close to Valencia, Spain. Ground measurements were taken concurrently to morning overpasses of the Envisat and Terra satellites during the summers of 2002-04. Although the variability of ground temperatures is smaller at night, satellite-derived LST products should be validated also at day-time since LST data are mostly required at day, e. g., for monitoring surface fluxes. The Valencia test site has been already used for the validation of the AATSR LST product (Prata, 2003; Coll et al., 2005).

In the present study, we used the ground measurements for the validation of LSTs derived from AATSR and MODIS data using split-window algorithms. Concurrent Terra/Advanced Spaceborne Thermal Emission Reflection Radiometer (ASTER) data were employed for analyzing the thermal homogeneity of the test site at a spatial scale resolution (90 m) smaller than AATSR and MODIS (1 km). Probably, split-window methods are the simplest approach for the derivation of LST and can be applied at global scale in an operational way. They are based on the atmospheric differential absorption in two adjacent channels in the 10 – 12.5 μm window. Although the split-window technique was initially used for the retrieval of the sea surface temperature (SST), it can be extended for land surfaces provided that emissivity effects are taken into account (Price, 1984; Becker and Li, 1990 and 1995; Coll and Caselles, 1997). The heterogeneity of land surfaces, both in temperature and emissivity, makes that LSTs are more difficult to estimate from satellite data than SSTs, and more difficult to validate with ground measurements.

This paper is organized as follows. The Valencia experimental site is described in section 2. Section 3 shows the methodology used for the ground measurements in the field campaigns. Then, the ground LST database is presented together with the list of concurrent satellite acquisitions that can be validated with the ground data. Section 4 gives a brief description of several split-window algorithms for LST applicable to AATSR and MODIS data. These algorithms were validated with the ground LSTs in section 5, where the results of the validation are shown and discussed. Finally, the conclusions are given in section 6.

2. THE VALENCIA EXPERIMENTAL SITE

An experimental site suitable for the validation of satellite-derived LSTs was set up in a large, flat and homogeneous area in the Mediterranean coast of Spain, close to the city of Valencia. The site is in a marshy plain surrounding the Albufera Lake and separated from the sea by a narrow strip of land. The area is shown in the color composite image of Fig. 1, which is a part of an ASTER scene taken on August 3, 2004. The region has been traditionally dedicated to the intensive cultivation of rice. From the end of June to the beginning of September, rice crops are well developed and attain nearly full cover. Crops are irrigated during the summer months, until harvest in mid September. In these circumstances, the site shows a high thermal homogeneity and is large enough for making ground measurements of LST comparable to satellite estimates. Only narrow tracks and irrigation channels cross the site, which facilitates the accessibility to the rice fields without breaking too much the homogeneity of the area. In addition, the emissivity of green vegetation with full cover is well known (high emissivity with small or null spectral variation between 8 and 13 μm; Salisbury and D'Aria, 1992; Rubio et al., 2003) thus facilitating the measurement of surface temperatures by means of TIR radiometers.

The ground LST measurements were performed in squares of 1 km^2 located in the southern part of the rice field area, where it has a maximum extension (see Fig. 1). In the campaigns of 2002 and 2003, the 1 km^2 test site was centered at 0º17'50''W, 39º14'27''N. For the 2004 campaign, the test site was moved 1 km North (center at 0º17'43"W, 39º15'01"N) because the new location was apparently more homogeneous in terms of rice plant development and growth this year. Figure 2 shows a map with the location of the 1 km^2 test sites. Cloud free atmospheric conditions are frequent in the area during the months of July and August. According to the atmospheric profile product of MODIS (MOD07), the total column content of atmospheric water vapor (or precipitable water) ranged between 1.5 cm and 3 cm for the days of the field campaigns.

In order to show the thermal homogeneity of the test site, we used the ASTER TIR data acquired over the area in August 3, 2004. Figure 3 shows a 10×10 km^2 image of brightness temperature in band 13 (10.66 μm). We selected 40 boxes of 11×11 pixels each (1 km^2, approximately) in the rice field area. For each box, the average temperature (T_{av}), the standard deviation (σ), and the difference between the maximum and the minimum temperature (T_M-T_m) were calculated. For the 40 boxes, T_{av} ranged from 26.6 ºC to 27.3 ºC, σ was between 0.23 ºC and 0.69 ºC and T_M-T_m between 1.0 ºC and 3.6 ºC. For comparison, the values for an area of 11×11 pixels at the nearby sea surface were T_{av}=24.44 ºC, σ=0.12 ºC, and T_M-T_m=0.71 ºC. The noise equivalent temperature difference of ASTER TIR bands is ≤0.3 ºC (Yamaguchi et al., 1998). In this analysis we did not consider the hot spot at 0º18'50''W, 39º14'30''N in Fig. 3, which is the largest temperature heterogeneity in the rice crop area. According to the temperatures and size of the hot spot, it could increase the 1 km^2 surface temperature by as much as 1 ºC with regard to the surrounding rice field temperatures. This effect was sometimes noticeable in the AATSR and MODIS images, so that the hot pixel could be removed for the comparison with the ground measurements.

Taking together the 40 boxes (4840 pixels), we obtained T_{av}=26.88 ºC, σ=0.43 ºC, and T_M-T_m=4.17 ºC. Figure 4 shows a histogram of the brightness temperatures for the 40 boxes. The largest temperatures (28.0 – 30.0 ºC) were for few pixels corresponding to roads that are visible in the southern part of the area. However, about 98 % of the pixels had temperatures between 26.0 ºC and 28.0 ºC. Similar results were obtained for the two 3×3 km^2 boxes (1089 pixels each) shown in Fig. 3: T_{av}=26.77 – 26.92 ºC, σ=0.41 – 0.45 ºC, and T_M-T_m=3.44 – 3.83 ºC, with more than 98 % of the pixels with temperatures between 26.0 ºC and 28.0 ºC. These results show that the experimental area contains a considerable number of 1 km^2 pixels for which the variability (σ) in surface temperature can be regarded as ≤0.5 ºC, approximately.

For the nadir view of AATSR, the instantaneous field of view (IFOV) is 1 km × 1 km at the center of the swath (Llewellyn-Jones et al., 2001). This is also the case for MODIS observations close to nadir. However, the IFOV grows considerably for off-nadir observations, especially in the across-track direction. According to Masuoka et al. (1998), the MODIS IFOV is 1.3 km (along-track) ×1.6 km (across-track) at scan angle of 35º (viewing angle of 40º, approximately), and 1.7 km × 3.3 km at scan angle of 50º (viewing angle of 60º). Taking into account that the spatial response function of MODIS detectors in the across-track direction is triangular covering twice of the IFOV (Barnes et al., 1998), the area contributing to the radiance of a MODIS pixel is approximately 1.3 km × 3.2 km at viewing angle of 40º, and 1.7 km × 6.6 km at viewing angle of 60º. Therefore, the cases for which the MODIS viewing angle is larger than 40º should be considered with care since they may be affected by larger uncertainties in the comparison with the ground measurements.

3. GROUND MEASUREMENTS

Ground temperatures were measured inside the 1 km^2 test site concurrently with daytime, cloud-free overpasses of the Envisat and Terra satellites during the summers of 2002-04. Table 1 shows the list of dates and the time intervals of the ground measurements with the concurrent overpass time of the AATSR and MODIS sensors. There are five days of AATSR/ground data concurrences for the 2002 campaign. The AATSR data were provided by the AATSR Validation Team, University of Leicester. In the case of MODIS, the overpass time was within the ground measurement window for a total of eleven days. All the concurrent MODIS scenes were acquired through the Earth Observing System Data Gateway at the web page edcimswww.cr.usgs.gov.

We used a total number of four thermal infrared radiometers for the ground measurements. The instruments were two CE 312 radiometers (CIMEL Electronique) with four bands (1 to 4 at 8-13 μm, 11.5-12.5 μm, 10.5-11.5 μm and 8.2-9.2 μm, respectively), one Everest model 112.2L thermometer with one single band (8-13 μm) and one AGA model 80 thermometer (single band, 8-13 μm). In the 2002 campaign one CE 312 radiometer (CE1), the Everest and the AGA instruments were used. In the 2003 campaign, the second CE 312 radiometer (CE2) was also available together with the previous three instruments. In the 2004 campaign, the two CE 312 and the Everest radiometers were used.

The CE 312 radiometers are radiance-based, self-calibrated instruments that allow compensation for the radiance of the detector's cavity (see Sicard et al., 1999, for details). Their accuracy was checked regularly during the field campaigns using a calibration blackbody. According to the calibration measurements, an absolute accuracy, σ(cal), of ±0.2 ºC (±0.1 ºC) was obtained for the four channels of CE1 (CE2). The Everest and AGA instruments have lower accuracies and may give biased LST measurements depending on the ambient operating temperature. We decided to use them in order to have a better estimate of the LST variability across the test site, but taking care of not introducing too much uncertainty in the measurements. With the aim of correcting the Everest and AGA measurements, blackbody calibration measurements were made before and after the transects each day of measurements. Additional calibration points covering a wider range of temperature were obtained for different targets (rice plants, water and bare soil) taking simultaneous measurements with the four instruments, band 1 of the CE 312 radiometers being the reference temperature. The calibration database was used to derive linear calibration equations that were updated with new data each day (see Coll et al., 2005, for more details). Such calibration equations were used to correct the bias in the Everest and AGA temperature readings. However, the calibrated temperatures still had relatively large dispersions, which were taken as the calibration accuracy, σ(cal) (typically, between ±0.5 and ±0.7 ºC for the Everest, and between ±0.7 and ±0.9 ºC for the AGA).

In order to capture the spatial variability of the surface temperature within the test site, each radiometer was assigned to one part of the 1 km^2 square (see Fig. 2). Radiometers were carried forth and back along transects of about 100 m length, looking at the surface at angles close to nadir. The field of view of the radiometers was 30 cm on the crop surface. Measurements were made at a rate of more than 5 measurements per minute, covering a distance of 30-50 m per minute. Data were collected during periods of 20-30 minutes centered at the satellite overpass time, although radiometers were in place and working 30 minutes before, in order to assure a good stability of their response. For each transect, we recorded the time of the individual measurement and the corresponding radiometric temperature. With these data we have obtained the ground LSTs to be compared with the satellite derived LSTs, as well as the spatial and temporal variability of LST at scales of 100 m for different parts (transects) of the 1 km^2 test site. The processing of the ground temperatures is described below.

3.1. Emissivity correction

Radiometric temperatures must be corrected for emissivity effects, including the reflection of the downward sky emission. If T_r is the radiometric temperature measured by a thermal infrared radiometer, the true land surface temperature T is given by

$$B(T)=[B(T_r)-(1-\varepsilon)L_{sky}]/\varepsilon \qquad (1)$$

where B is the Planck function weighted for the filter of the radiometer, ε is the surface emissivity and L_{sky} is the downward sky irradiance (F_{sky}) divided by π. The surface emissivity was measured in the field using the box method (Rubio et al., 2003). These measurements showed a high emissivity (ε=0.985) with negligible spectral variation (Coll et al., 2005), which is typical for green vegetation with full cover (Salisbury and D'Aria, 1992; Rubio et al., 2003). The downward sky radiance was measured at an angle of 53º from nadir, which is equivalent to F_{sky}/π according to the diffusive approximation for clear skies (Kondratyev, 1969). These measurements were performed with each radiometer at the start and the end of the temperature transects. Then, the true LSTs can be calculated from the radiometric temperatures according to Eq. (1) and inverting the weighted Planck function. For ε=0.985 the difference $T-T_r$ (i.e., the emissivity correction for the radiometric temperatures) ranged between 0.3 ºC and 0.6 ºC, depending on the magnitude of L_{sky}. The uncertainty associated to this process is mainly due to the error in the emissivity value used. For an error of ±0.010 in emissivity, the resulting error in temperature, σ(em), ranged from ±0.2 ºC to ±0.4 ºC, depending on L_{sky}. The impact of the person carrying the radiometer on the radiation reflected at the surface (which affects L_{sky} in Eq. 2) was evaluated to be 0.1 ºC or less for our conditions of measurement.

3.2. Averaging of ground temperatures for each transect

We considered only the temperatures measured within 3 minutes around the satellite overpass time (more than 20 temperature measurements covering a distance of about 100 m, for each transect) for comparison with the satellite derived LSTs. These data were averaged for each transect/radiometer and the standard deviation was calculated. It gives us an estimation of the LST spatial and temporal variability in a part of the test site, σ(var). For the data analyzed here, σ(var) was between ±0.3 ºC and ±0.5 ºC for both CE 312 radiometers, with similar values for the Everest and AGA.

Moreover, we also considered the variability of LST for the whole measurement period in order to check the consistency of the ground data. For all the dates, we have found no apparent temporal trend in temperature during the ~20 minute periods. The average LST for the whole period differed from the 3-minute average LST by only 0.0 – 0.3 ºC for most of the days. For the whole period, σ(var) ranged between ±0.4 ºC and ±0.7 ºC, comparable to the values for the 3 minute period mentioned above. As seen in Table 1, the measurement interval for 12/08/2003 ended few minutes before the satellite overpass. Therefore, we could not take the average LST for the 3 minute period around the overpass time. Instead, we considered the whole measurement period for the average LST and σ(var) on this date (no long-term variability was observed in the ground temperatures).

The total uncertainty in the temperature measurement for each radiometer, σ(T), is given by the combination of the three sources of error (calibration, emissivity correction and spatial/temporal variability) according to

$$\sigma(T) = [\sigma(cal)^2+\sigma(em)^2+\sigma(var)^2]^{1/2} \qquad (2)$$

For each day of measurement, we have 2-4 values of ground LST (one for each radiometer/transect), with their corresponding uncertainties. Tables 2 and 3 give the data corresponding to the AATSR and MODIS overpasses of Table 1, respectively. The accuracy of the ground LSTs measured by the CE1 and CE2 radiometers was in the range between ±0.3 ºC and ±0.6 ºC for most of the dates. The largest part of this error was due to the natural variability of surface temperatures, σ(var). For the dates when the two CE 312 instruments were available, the maximum difference between their measured LSTs was 1.1 ºC. In the case of the Everest and AGA instruments, the calibration error, σ(cal), was usually the largest source of error (σ(var) being similar to that of CE1 and CE2). In order to avoid excessive uncertainty due to the calibration problems of the Everest and AGA instruments, we kept only their LST data with $\sigma(T) \leq 1.0$ ºC. In addition, we removed all LSTs measured by these instruments that differed by more than 1.0 ºC from any of the CE 312 LSTs on the same day. As shown in Table 3, Everest and AGA were seldom used in the 2004 campaign.

3.3. Average ground LST

The ground LSTs to be compared with AATSR and MODIS derived LSTs at 1 km^2 resolution were calculated by averaging all the individual ground temperatures within the 3 minute periods for the available radiometers each measurement day. In this average, less weight was given to the Everest and AGA readings since they are typically less in number (owing to a smaller sampling frequency compared with CE1 and CE2). The error associated with the average LST was calculated with Eq. (2), including σ(var) for all the individual temperatures averaged, the emissivity correction error, and the calibration error for each instrument. The average LSTs and uncertainties concurrent to the AATSR and MODIS overpasses are given in the last column of Tables 2 and 3, respectively. The range of the ground LSTs was from 25 ºC to 32 ºC, with uncertainties between ±0.5 ºC and ±0.9 ºC. This accuracy interval may not be valid enough for the vicarious calibration of TIR satellite radiometers, but we consider that it could be useful for the validation of operational LST products derived from satellite data in real conditions.

4. SPLIT-WINDOW ALGORITHMS FOR LST

In this section, we briefly describe the different split-window formulations for LST retrieval to be validated with ground data in section 5. They are (1) the algorithm used for the derivation of the AATSR LST data product, (2) the MODIS generalized split-window algorithm used to generate the MOD11_L2 LST product, and (3) a quadratic, emissivity dependent split-window algorithm applicable to both AATSR and MODIS data.

4.1.- AATSR LST algorithm

Although the AATSR was primarily designed to obtain accurate sea surface temperatures (Llewellyn-Jones et al., 2001), it can be also applied for the retrieval of LSTs. The AATSR LST algorithm (Prata, 2000) uses the brightness temperatures at 11 μm and 12 μm, T_{11} and T_{12}, for the nadir view of AATSR. Basically the algorithm expresses the LST as a linear combination of the brightness temperatures T_{11} and T_{12} with the coefficients being determined by regression using simulated data-sets and depending on the land cover type (i), the fractional vegetation cover (f), the precipitable water (pw) and the satellite zenith viewing angle (θ). It should be noted that the algorithm has no explicit dependence on surface emissivity. The effects of surface emissivity are implicitly taken into account through the land cover type and fractional cover dependent coefficients. The algorithm can be written as

$$LST = a_{f,i,pw} + b_{f,i}(T_{11}-T_{12})^n + (b_{f,i} + c_{f,i})T_{12} \quad (3)$$

where $n=\cos(\theta/5)$ is approximately equal to 1 since $\theta<23.5°$ for the nadir view. (In fact, using $n=1$ in Eq. (3) instead of the exact value of n implies a very small difference in LST: for $\theta=23.5°$, we have $n=0.9966$, which yields a LST difference lower than 0.04 ºC for $T_{11}-T_{12}=3$ ºC.) The coefficients of Eq. (3) are given by:

$a_{f,i,pw} = 0.4[\sec(\theta)-1]pw + f\, a_{v,i} + (1-f)\, a_{s,i}$

$b_{f,i} = f\, b_{v,i} + (1-f)\, b_{s,i}$

$c_{f,i} = f\, c_{v,i} + (1-f)\, c_{s,i}$

These coefficients have been calculated for the 13 different biomes or land cover classes (i=1 to 13) defined by Dorman and Sellers (1989). For a given land cover class, two separate sets of coefficients are given for the fully vegetated surface (subscript v) and for the bare surface (subscript s), which are weighted by the fractional vegetation cover f. The precipitable water (pw, in cm or g/cm^2) is obtained from climatologic data. It is only required for the term $0.4[\sec(\theta)-1]pw$ in coefficient $a_{f,i,pw}$ and has a small impact on LST: since $\theta<23.5°$ for the AATSR nadir view, $\partial LST/\partial pw=0.4[\sec(\theta)-1]$ is always smaller than 0.04 ºC/cm. The AATSR LST algorithm is operationally implemented at the Rutherford Appleton Laboratory (RAL) in the so-called RAL processor. It uses the last version of the split-window coefficients (Prata, 2002). The values of i, f and pw required for the application of the algorithm are obtained from global classification, fractional vegetation cover maps and global climatology at a spatial resolution of 0.5º×0.5º longitude/latitude. Monthly variability is allowed for f and pw. LST images produced with this algorithm are currently provided with AATSR_L2 data.

Since the 0.5º grid cell is too coarse in order to properly assign split-window coefficients to specific, relatively small areas such as our test site, we implemented ourselves the LST algorithm to the AATSR brightness temperatures T_{11} and T_{12} from AATSR L1b data for our test area only. Thus, we selected land cover class i=6 (broadleaf trees with groundcover, which is the class assigned to our site by the RAL processor) with f=1 (full vegetation cover) which is appropriate for the fully developed rice crops in summer (the RAL processor assigned f=0.40 – 0.47 in July and August). Using the last available version of the coefficients, the AATSR LST equation locally tuned to our study areas is

$$LST = 0.4[\sec(\theta)-1]pw + 0.9089 + 3.3511(T_{11}-T_{12})^n + 0.9621T_{12} \quad (4)$$

with LST, T_{11} and T_{12} in ºC. The precipitable water was taken pw=2.5 cm for midlatitude summer conditions. The impact of pw in LST is very small for the viewing angles of the AATSR nadir view, as mentioned above.

4.2.- MODIS generalized split-window algorithm

The generalized split-window algorithm applied to the MODIS brightness temperatures in channels 31 (10.78 – 11.28μm) and 32 (11.77 – 12.27μm), T_{31} and T_{32}, can be written as (Wan and Dozier, 1996)

$$LST = C + \left(A_1 + A_2\frac{1-\varepsilon}{\varepsilon} + A_3\frac{\Delta\varepsilon}{\varepsilon^2}\right)\frac{T_{31}+T_{32}}{2} + \left(B_1 + B_2\frac{1-\varepsilon}{\varepsilon} + B_3\frac{\Delta\varepsilon}{\varepsilon^2}\right)\frac{T_{31}-T_{32}}{2} \quad (5)$$

where $\varepsilon=(\varepsilon_{31}+\varepsilon_{32})/2$ and $\Delta\varepsilon=\varepsilon_{31}-\varepsilon_{32}$ are, respectively, the mean emissivity and the emissivity difference in MODIS channels 31 and 32. Coefficients C, A_i and B_i were obtained from linear regression of MODIS simulated data for wide ranges of surface and atmospheric conditions, and they depend on the view angle, the column water vapor content and the atmospheric lower boundary temperature. The required emissivities are obtained form classification-based emissivities (Snyder at al., 1998), which have been modeled for 14 different land cover types. For each MODIS pixel, the land cover class is assigned according to the classification given by the MODIS land-cover product. The LST generated with the generalized split-window algorithm is provided in the MODIS product MOD11_L2 (Wan et al. 2002).

4.3.- Quadratic, emissivity dependent split-window algorithm

The LST split-window algorithm of Coll and Caselles (1997) has an explicit dependence on surface emissivity. For two generic channels at 11 μm and 12 μm, channels 1 and 2 respectively, and using the mean emissivity, $\varepsilon=(\varepsilon_1+\varepsilon_2)/2$, and the channel emissivity difference, $\Delta\varepsilon=\varepsilon_1-\varepsilon_2$, the algorithm can be written as

$$LST = T_1 + a_0 + a_1(T_1-T_2) + a_2(T_1-T_2)^2 + \alpha(1-\varepsilon) - \beta\Delta\varepsilon \quad (6)$$

where coefficients a_0, a_1, a_2, α and β depend on the particular split-window channels used, coefficient β depending also on the precipitable water. This algorithm was applied and validated with NOAA/AVHRR data in Coll and Caselles (1997) and with GMS-5 VISSR data in Prata and Cechet (1999). It has a quadratic dependence on the brightness temperature difference (T_1-T_2) in order to account for the increase of the atmospheric correction for large amounts of atmospheric water vapor.

For the full cover rice crops of the Valencia test site, we can expect a high value of surface emissivity with no spectral variation in the spectral band between 10.5 μm and 12.5 μm. Based on the emissivity measurements performed in the site, we can take ε=0.985 and $\Delta\varepsilon$=0 (Coll et al., 2005). In the case of AATSR, we used the values for the coefficients of Eq. (6) given by Sòria et al. (2002). These coefficients were calculated from a regression analysis over a database of simulated top-of-the-atmosphere AATSR radiances covering global surface and atmospheric conditions. The AATSR algorithm can be written specifically for the test site (ε=0.985; $\Delta\varepsilon$=0) as

$$LST = T_{11} + 0.57 + 1.03(T_{11}-T_{12}) + 0.26(T_{11}-T_{12})^2 \qquad (7)$$

Similarly, the coefficients for Eq. (6) appropriate for MODIS were taken from Sobrino et al. (2003), which were also obtained from regression analysis over a simulated database of MODIS radiances covering worldwide conditions. With these coefficients and taking ε=0.985 and $\Delta\varepsilon$=0, the MODIS algorithm is

$$LST = T_{31} + 1.52 + 1.79(T_{31}-T_{32}) + 1.20(T_{31}-T_{32})^2 \qquad (8)$$

5. RESULTS AND DISCUSSION

For AATSR, we tested three split-window equations: (1) the AATSR LST algorithm (Eq. 3) as applied operationally at RAL (i.e., the RAL processor), and provided as a product in the AATSR_L2 data; (2) the AATSR LST algorithm specific for the test site, i.e. Eq. (4), which was applied to brightness temperatures from AATSR_L1b data; and (3) the quadratic, emissivity dependent algorithm given by Eq. (7), also applied to AATSR_L1b data. For MODIS, we checked two formulations: (1) the generalized split-window algorithm (Eq. 5) as given by the MOD11_L2 product; and (2) the quadratic, emissivity dependent algorithm given by Eq. (8) applied to MODIS L1b data.

For each day with concurrent satellite data and ground LSTs, the satellite brightness temperatures for the split-window channels (T_{11} and T_{12}, nadir view, for AATSR; T_{31} and T_{32} for MODIS) corresponding to the test site were interpolated from the four pixels closest to the center of the test site, according to Wan et al. (2002). The interpolated brightness temperatures and the standard deviation (σ) of the four temperatures used are given in Table 4 for AATSR and Table 5 for MODIS, together with the satellite viewing zenith angle (θ). In Table 5, the atmospheric precipitable water (pw) obtained from the MODIS atmospheric profile product (MOD07) is also shown. According to Table 4, the standard deviation of the AATSR brightness temperatures was always smaller than 0.1 ºC, and observation was close to nadir ($\theta \leq 16^{\circ}$). MODIS covers a wider range of viewing angles (up to 60º for our data). For low θ, the standard deviation of the MODIS brightness temperatures was similar to that of AATSR. The largest values of σ were generally associated with the largest viewing angles; however, $\sigma \leq 0.3$ ºC for most of the cases. These results show a good thermal homogeneity of the test area at the AATSR and MODIS spatial scale. Nevertheless, special care should be taken in the case of large observation angles, for which the uncertainty in the comparison with the ground LST could be larger than for nadir observation. On the other hand, the brightness temperature difference (T_{11}-T_{12} or T_{31}-T_{32}), which plays an important role in the split-window algorithms, was between 1.87 ºC and 3.03 ºC for AATSR, and between 0.45 ºC and 1.56 ºC for MODIS.

The results of the comparison between the ground LSTs and the split-window LSTs are shown in Table 6 for AATSR and in Table 7 for MODIS. For each date, the average ground LST (from Table 2 for AATSR and from Table 3 for MODIS) is given together with the AATSR or MODIS derived LSTs. For each of the algorithms, we give the LST for the test site interpolated from the four neighboring pixels, and the difference between the ground and the algorithm LST.

Although the number of data available for the LST comparison was rather limited, some conclusions can be drawn from these results. Regarding to AATSR, the LSTs obtained from the RAL processor seem to overestimate the ground LSTs by 3 ºC in average. However, the LSTs calculated with Eq. (4) show a better agreement with the ground data, with a maximum difference of –2.0 ºC, an average difference or bias of –0.9 ºC, and a standard deviation of 0.9 ºC. As mentioned before, the RAL processor assigns the split-window coefficients based on global classification and fractional vegetation cover maps at a spatial resolution of 0.5º×0.5º longitude/latitude (for the Valencia test site, i=6; broadleaf trees with ground cover, and f=0.40 – 0.47

in July and August). The only difference in Eq. (4) is that we used f=1, which is more appropriate for our test area and yields better results for LST. In order to check the sensitivity of the AATSR LST algorithm to the split-window coefficients, various sets of coefficients for different land cover types were used with f=1 and pw=2.5 cm. The best results were found for i=5 (needleleaf deciduous trees), with a maximum difference with regard to the ground LST of 1.3 ºC, average bias of 0.0 ºC and a standard deviation of 0.9 ºC. Also, for i=8 (broadleaf shrubs with groundcover), the maximum difference was 1.6 ºC, the bias was 0.3 ºC and the standard deviation was 0.9 ºC. These results are comparable to those of Eq. (4), which points out the consistence of the AATSR LST algorithm. On the other hand, the quadratic, emissivity dependent LST algorithm of Eq. (7) yielded also a good agreement with the ground data (maximum difference of 1.6 ºC, average bias of 0.3 ºC and standard deviation of 0.9 ºC). The results of the simple algorithm of Eq. (7), as well as those of Eq. (4), give confidence to the use of split-window methods for the retrieval of LST from AATSR data.

With regard to MODIS, the MOD11 LST product showed a good agreement with the ground LST, with differences around or smaller than the ground measurements errors for most of the dates. It should be noted that, as mentioned in section 4.2, the emissivities for the generalized split-window algorithm used by MODIS (Eq. 5) are assigned on a pixel by pixel basis, which allows a good representation of the variability of surface types across a scene. Taking the eleven data of Table 7, the MOD11 LST yielded an average bias of 0.6 ºC and standard deviation of 0.9 ºC. The maximum differences with regard to the ground LST were around 2 ºC for days 26/07/02 and 26/08/03. The reason for such big discrepancies was investigated by looking at the correlation between the brightness temperature difference, T_{31}-T_{32}, and the precipitable water along the MODIS viewing direction, pw/cosθ, which can be obtained from the data of Table 5. For these two days, T_{31}-T_{32} was the highest (1.4 – 1.6 ºC) while pw/cosθ had moderate values (3.0 – 3.9 cm, for a total range of 1.7 – 4.5 cm). The anomalous large values of T_{31}-T_{32} for the two cases could be due to invisible cirrus clouds (Wan, personal communication). If these two days were not considered, the average bias of MOD11 was 0.3 ºC with a standard deviation of 0.7 ºC. Additionally, the viewing angle was very large (θ>60º) for days 08/07/03 and 09/08/03. Removing these dates also, the average bias was 0.1 ºC and the standard deviation was 0.6 ºC. The maximum difference was 1.4 ºC for 10/07/02; however, the uncertainty in the ground measurements for this day was large since, as shown in Table 3, only two instruments (CE1 and Everest) were used and they differed by 1 ºC. On the other hand, the quadratic algorithm of Eq. (8) yielded excellent results when compared with the ground LSTs: a maximum difference of -1.0 ºC, a bias of 0.0 ºC and a standard deviation of 0.5 ºC.

As shown in Table 5, the MODIS data encompass viewing angles from close to nadir to 60º. Ground LST measurements were performed close to nadir, so there may be any discrepancy when compared with satellite measurements at large viewing angles. However, the angular variations of LST for the unstressed, fully-covering rice crop are expected to be small. According to the experimental results of Lagouarde et al. (1995) for alfalfa, the differences between the nadir and off-nadir (±60º) brightness temperatures were within ±0.5 ºC. Such small variation was attributed to the high density of the canopy (as in our case, the soil was not visible) and the absence of water stress, which is likely to reduce the angular effects (Fuchs, 1990). The differences between the ground and the algorithm LST (ΔT) are plotted against the satellite viewing angle in Fig. 5 for the MODIS data. This plot suggests a variation of ΔT with the viewing angle with amplitude of about 1 ºC, for both the MOD11_L2 data (excluding the two data with cirrus clouds) and Eq. (8), which could be compatible with the above mentioned angular variations. The observed increase of ΔT with θ may suggest a small decrease of the ground LST for off-nadir observation, in concordance with the measurements shown by Lagouarde et al. (1995) for alfalfa at high solar elevations. On the other hand, the positive values of ΔT could be due to an insufficient correction of the atmospheric absorption for large water vapor loads. In Fig. 6, ΔT is plotted against the satellite brightness temperature difference, T_{31}-T_{32}. For the MOD11_L2 data, the correlation between ΔT and T_{31}-T_{32} is high (r=0.87) and the algorithm underestimates the ground LST for large values of T_{31}-T_{32} (i.e., when the atmospheric correction should be larger) while its performance is better for the lower values of T_{31}-T_{32}. If we consider only the validation data with T_{31}-T_{32}<1.0 ºC (7 data), the MOD11_L2 temperatures yield a mean bias of -0.1 ºC and a standard deviation of 0.6 ºC with regard to the ground LSTs. For the quadratic split-window algorithm of Eq. (8), it is not observed any correlation between ΔT and T_{31}-T_{32}. This shows that the quadratic dependence on the brightness temperature difference is adequately accounting for the increased atmospheric correction at large values of T_{31}-T_{32}. However, this algorithm should be further validated in a wider temperature range, especially at high LST cases (>50 ºC), where the quadratic term may give larger errors.

6. SUMMARY AND CONCLUSIONS

A database of ground measurements of temperature was collected in the Valencia test site for the validation of LSTs derived from concurrent satellite data. The test site and the methodology followed for the ground measurements are described in this paper. Ground temperatures corresponding to Envisat/AATSR and Terra/MODIS morning overpasses were obtained with an estimated accuracy between ±0.5 ºC and ±0.9 ºC, the largest part of these uncertainties being due to the spatial variability of surface temperature. The ground database was used for the validation of LSTs derived from AATSR and MODIS data using various split-window algorithms. The operational LST split-window algorithms for AATSR (Prata, 2000) and MODIS (Wan and Dozier, 1996) were checked, as well as the quadratic, emissivity dependent algorithm of Coll and Caselles (1997), with coefficients adapted for the AATSR and MODIS split-window channels.

Results indicate an overestimation of about 3 ºC for the LST provided by the AATSR RAL processor in the L2 image files. It appears that the 0.5º resolution of land cover type and vegetation fraction maps used for the assignation of split-window coefficients is too coarse for areas such as our test site. The AATSR LST algorithm is very sensitive to vegetation fraction: when applied with f=1, the agreement with the ground data was better, with a mean difference (ground minus algorithm) of -0.9 ºC and a standard deviation of 0.9 ºC. The MODIS LST product (MOD11_L2), which uses split-window coefficients assigned according to the MODIS land cover product at one pixel resolution, yielded good results when compared with the ground data, with differences comparable or smaller than the uncertainties of the ground measurements for most of the dates. For the cloud-free cases and $\theta<60^{\circ}$, the MOD11_L2 algorithm yielded an average underestimation of 0.1 ºC and standard deviation of 0.6 ºC. The quadratic algorithm showed a good performance for both AATSR and MODIS data, giving differences with the ground LSTs within ±1.0 ºC for most of the days and the smallest average biases (+0.3 ºC for AATSR and 0.0 ºC for MODIS). Although the number of validation data is rather small and limited to the case of a fully vegetated surface with ground LSTs ranging from 25 to 32 ºC and in conditions of moderate loads of atmospheric water vapor (1.5 – 3 cm), these results give confidence to the LSTs derived by means of split-window methods. We expect to augment the number of validation data in the Valencia test site in future campaigns, both for day and night. More TIR radiometers will be used in order to better characterize the spatial variability of LST at the site.

ACKNOWLEDGEMENTS

This work has been financed by the *Ministerio de Ciencia y Tecnología* (*Acción Especial* REN2002-11605-E/CLI; Project REN2001-3116/CLI, and *"Ramón y Cajal"* Research Contract of Dr. E. Valor), the *Ministerio de Educación y Ciencia* (Project CGL2004-06099-C03-01, *Acción Complementaria* CGL2004-0166-E and Research Grant of Dr. R. Niclòs), the *AlBan programme* of the European Union (Research Grant of Dr. R. Rivas) and the University of Valencia (*V Segles* Research Grant of Mr. J. M. Sánchez). NASA (Project EOS/03-

0043-0379) is also acknowledged. We wish to thank the AATSR Validation Team and the EOS Data Gateway for providing the satellite data. Fruitful discussions and suggestions from Dr. Zhengming Wan (UCSB) are greatly appreciated.

REFERENCES

Barnes, W., L., Pagano, T. S. and Salomonson, V.V. (1998). Prelaunch characteristics of the Moderate Resolution Imaging Spectroradiometer (MODIS) on EOS-AM1. *IEEE Transactions on Geoscience and Remote Sensing*, 36, 1088-1100.

Becker, F. and Li, Z.-L. (1990). Towards a local split-window method over land surfaces. *International Journal of Remote Sensing*, 11, 369-394.

Becker, F. and Li, Z.-L. (1995). Surface temperature and emissivity at various scales: definition, measurement and related problems. *Remote Sensing Reviews*, 12, 225-253.

Coll, C. and Caselles, V. (1997). A global split-window algorithm for land surface temperature from AVHRR data: Validation and algorithm comparison. *Journal of Geophysical Research*, 102D, 16697-16713.

Coll, C., Valor, E., Caselles, V., Niclòs, R., Rivas, R., Sánchez, J. M. and Galve, J. M. (2005). Evaluation of the Envisat-AATSR land surface temperature algorithm with ground measurements in the Valencia test site. *Proceedings of the Envisat Symposium*, 6-10 September 2004, Salzburg, Austria (in press).

Dash, P., Göttsche, F.M., Olesen, F.S., and Fischer, H. (2002). Land surface temperature and emissivity estimation from passive sensor data: theory and practice –current trends. *International Journal of Remote Sensing*, 23 (13), 2563-2594.

Dorman, J. L. and Sellers, P. J. (1989). A global climatology for albedo, roughness length and stomatal resistance for atmospheric general circulation models as represented by the simple biosphere model (SiB). *Journal of Applied Meteorology*, 28, 833-855.

Fuchs, M. (1990). Infrared measurements of canopy temperature and detection of plant water stress. *Theoretical and Applied Climatology*, 42, 253-261.

Kondratyev, K. Ya. (1969). *Radiation in the Atmosphere*, Academic Press, New York.

Lagouarde, J. P., Kerr, Y. H. and Brunet, Y. (1995). An experimental study of angular effects on surface temperature for various plant canopies and bare soils. *Agricultural and Forest Meteorology*, 77, 167-190.

Llewellyn-Jones, D., Edwards, M. C., Mutlow, C. T., Birks, A. R., Barton, I. J. and Tait, H. (2001). AATSR: Global-change and Surface-Temperature measurements from ENVISAT. *ESA Bulletin*, February 2001, 11-21.

Masuoka, E., Fleig, A., Wolfe, R. E. and Patt, F. (1998). Key characteristics of MODIS data products. *IEEE Transactions on Geoscience and Remote Sensing*, 36 (4), 1313-1323.

Prata, A. J. (1994). Land surface temperatures derived from the Advanced Very High Resolution Radiometer and the Along Track Scanning Radiometer. II. Experimental results and validation of AVHRR algorithms. *Journal of Geophysical Research*, 99D, 13025-13058.

Prata, A. J. (2000). Land surface temperature measurement from space: AATSR Algorithm Theoretical Basis Document. *Technical Report*, CSIRO, 27 pp.

Prata, A. J. (2002). Land surface temperature measurement from space: Global surface temperature simulations for the AATSR. *Technical Report*, CSIRO, 15 pp.

Prata, A. J. (2003). Land surface temperature measurement from space: Validation of the AATSR Land Surface Temperature product. *Technical Report*, CSIRO, 40 pp.

Prata, A. J. and Cechet, R. P. (1999). An assessment of the accuracy of land surface temperature determination from the GMS-5 VISSR. *Remote Sensing of Environment*, 67, 1-14.

Price, J. C. (1984). Land surface temperature measurements from the split-window channels of the NOAA 7 AVHRR. *Journal of Geophysical Research*, 89(D5), 7231-7237.

Rubio, E., Caselles, V., Coll, C., Valor, E. and Sospedra, F. (2003). Thermal-infrared emissivities of natural surfaces: Improvements on the experimental set-up and new measurements. *International Journal of Remote Sensing*, 24 (24), 5379-5390.

Salisbury, J. W. and D'Aria, D. M. (1992). Emissivity of terrestrial materials in the 8-14 μm atmospheric window. *Remote Sensing of Environment*, 42, 83-106.

Sicard, M., Spyak, P. R., Brogniez, G., Legrand, M., Abuhassan, N. K., Pietras, C., and Buis, J. P. (1999). Thermal infrared field radiometer for vicarious cross-calibration: characterization and comparisons with other field instruments. *Optical Engineering*, 38 (2), 345-356.

Slater, P., Bigger, S. F., Thome, K., Gellman, D. I., and Spyak, P. R. (1996). Vicarious radiometric calibration of EOS sensors. *Journal of Atmospheric and Oceanic Technology*, 13, 349-359.

Snyder, W.C., Wan, Z., Zhang, Y., and Feng, Y.-Z. (1998). Classification-based emissivity for land surface temperature from space. *International Journal of Remote Sensing*, 19, 2753-2774.

Sobrino, J. A., El Kharraz, J. and Li, Z.-L. (2003). Surface temperature and water vapour retrieval from MODIS data. *International Journal of Remote Sensing*, 24 (24), 5161-5182.

Sòria, G., Sobrino, J. A., Cuenca, J., Prata, A. J., Jiménez-Muñoz, J. C., Gómez, M., and El-Kharraz, J. (2002). Surface temperature retrieval from AATSR data: multichannel and multiangle algorithms. *Proceedings of Recent Advances in Quantitative Remote Sensing*, University of Valencia, pp. 952-955.

Wan, Z. and Dozier, J. (1996). A generalized split-window algorithm for retrieving land surface temperature from space. *IEEE Transactions on Geoscience and Remote Sensing*, 34 (4), 892-905.

Wan, Z., Zhang, Y., Zhang, Q. and Li, Z.-L. (2002). Validation of the land-surface temperature products retrieved from Terra Moderate Resolution Imaging Spectroradiometer data. *Remote Sensing of Environment*, 83, 163-180.

Wan, Z., Zhang, Y., Zhang, Q. and Li, Z.-L. (2004). Quality assessment and validation of the MODIS global land surface temperature. International Journal of Remote Sensing, 25 (1), 261-274.

Yamaguchi, Y., Kahle, A. B., Tsu, H., Kawakami, T., and Pniel, M. (1998). Overview of Advanced Spaceborne Thermal Emission and Reflection Radiometer (ASTER). *IEEE Transactions on Geoscience and Remote Sensing*, 36, 1062-1071.

FIGURE CAPTIONS

Figure 1. ASTER color composite of the Valencia experimental site and environs, August 3, 2004. The two test sites (1 km^2 squares) are indicated. The RGB components are bands 3 (0.81 μm), 2 (0.66 μm) and 1 (0.56 μm), respectively.

Figure 2. Map of the area with the two 1 km^2 test sites (UTM-Zone 30 coordinates, in meters). The position of the TIR radiometers (CE 1, CE 2, Everest and AGA) is shown (*: 2003 campaign only). The center of test site 1 is at 733266E, 4347050N (0º17’50’’W, 39º14’27’’N). The center of test site 2 is at 733397E, 4348412N (0º17’43’’W, 39º15’01’’N).

Figure 3. Brightness temperature image (10×10 km^2) from ASTER band 13 (10.66 μm), August 3, 2004. The center of the two test sites is indicated with stars. Dashed (solid) squares represent 1 km^2 (3×3 km^2).

Figure 4. Histogram of brightness temperatures for the 40 boxes of 11×11 pixels in the rice field area.

Figure 5. Temperature difference ΔT (ground minus algorithm LST) against the zenith viewing angle, for the two MODIS LST algorithms (MOD11_L2 and Eq. 8).

Figure 6. Temperature difference ΔT (ground minus algorithm LST) against the brightness temperature difference T_{31}-T_{32}, for the two MODIS LST algorithms (MOD11_L2 and Eq. 8). For MOD11_L2, cases with zenith viewing angle smaller than or larger than 40º are indicated.

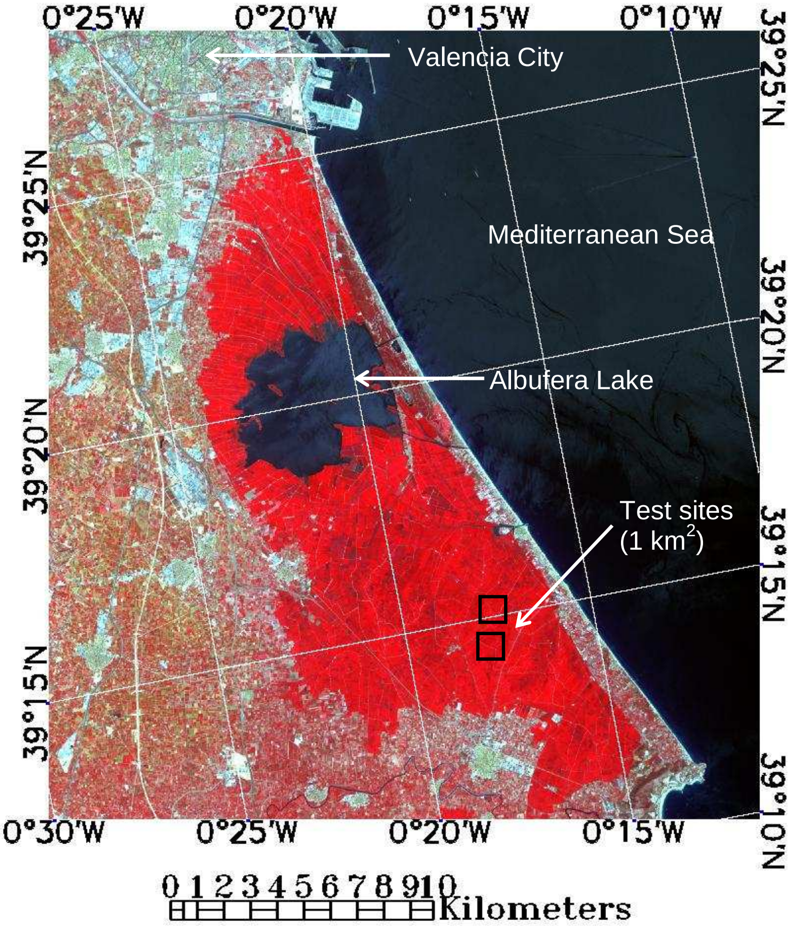

Figure 1. ASTER color composite of the Valencia experimental site and environs, August 3, 2004. The two test sites (1 km^2 squares) are indicated. The RGB components are bands 3 (0.81 μm), 2 (0.66 μm) and 1 (0.56 μm), respectively.

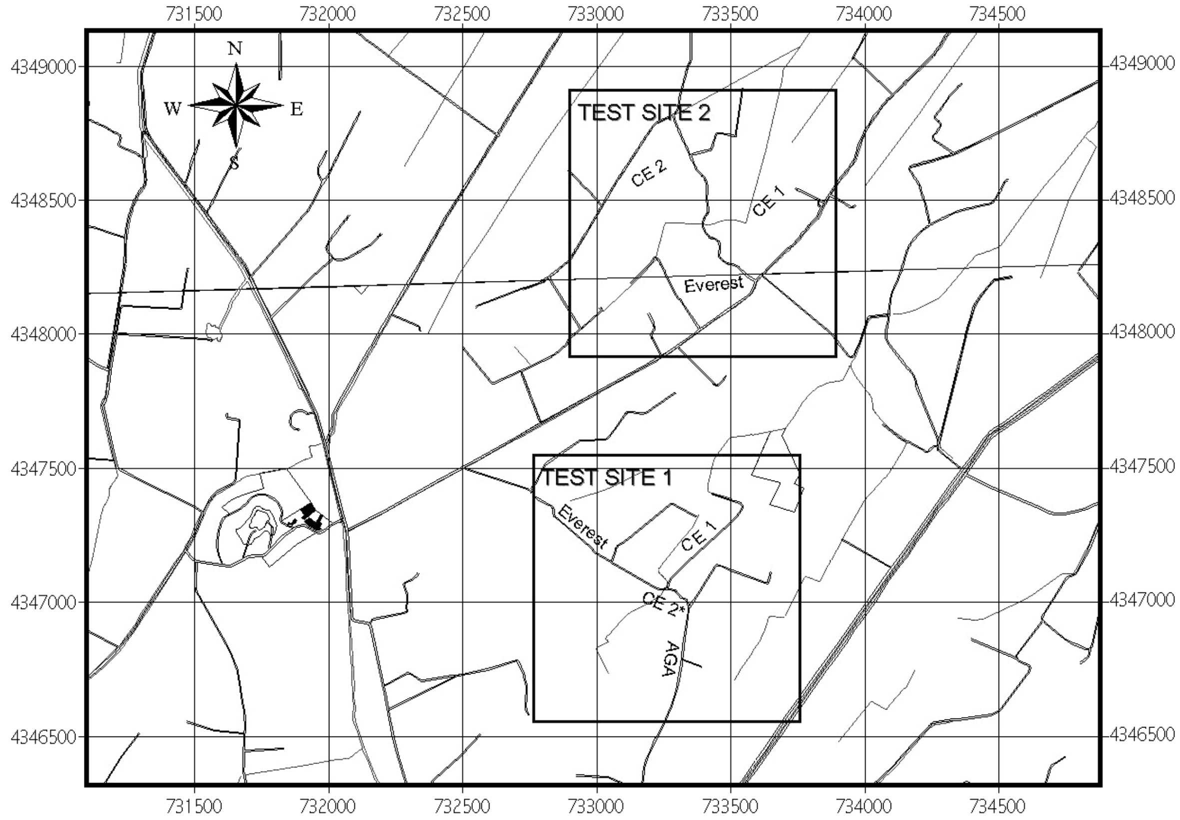

Figure 2. Map of the area with the two 1 km^2 test sites (UTM-Zone 30 coordinates, in meters). The position of the TIR radiometers (CE 1, CE 2, Everest and AGA) is shown (*: 2003 campaign only). The center of test site 1 is at 733266E, 4347050N (0º17'50''W, 39º14'27''N). The center of test site 2 is at 733397E, 4348412N (0º17'43''W, 39º15'01''N).

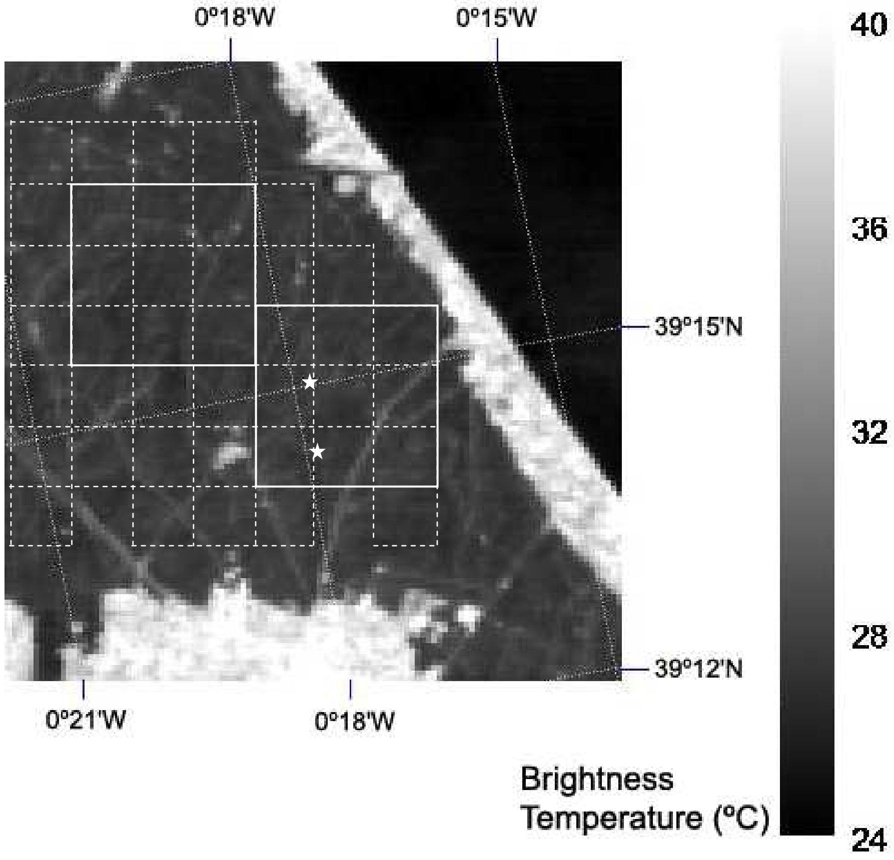

Figure 3. Brightness temperature image (10×10 km^2) from ASTER band 13 (10.66 μm), August 3, 2004. The center of the two test sites is indicated with stars. Dashed (solid) squares represent 1 km^2 (3×3 km^2).

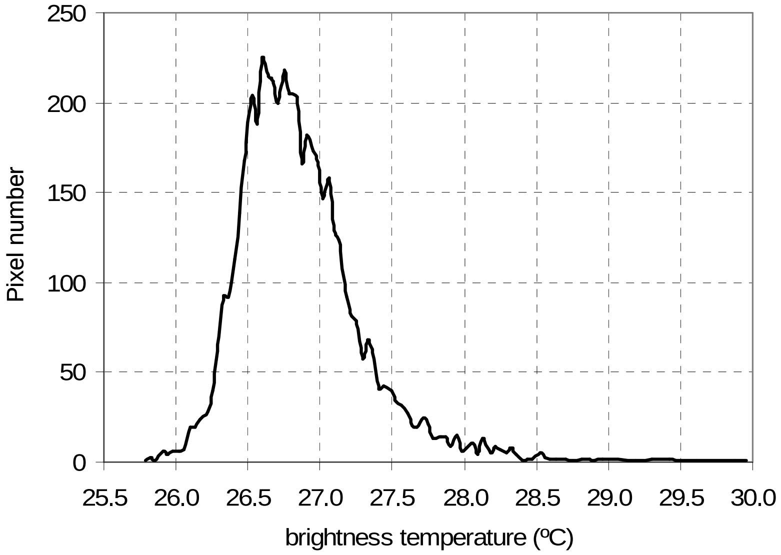

Figure 4. Histogram of brightness temperatures for the 40 boxes of 11×11 pixels in the rice field area.

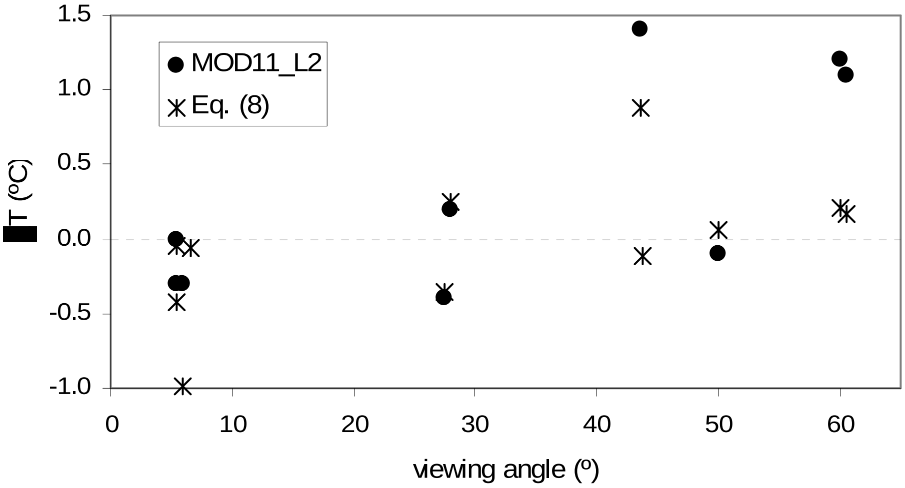

Figure 5. Temperature difference ΔT (ground minus algorithm LST) against the zenith viewing angle, for the two MODIS LST algorithms (MOD11_L2 and Eq. 8).

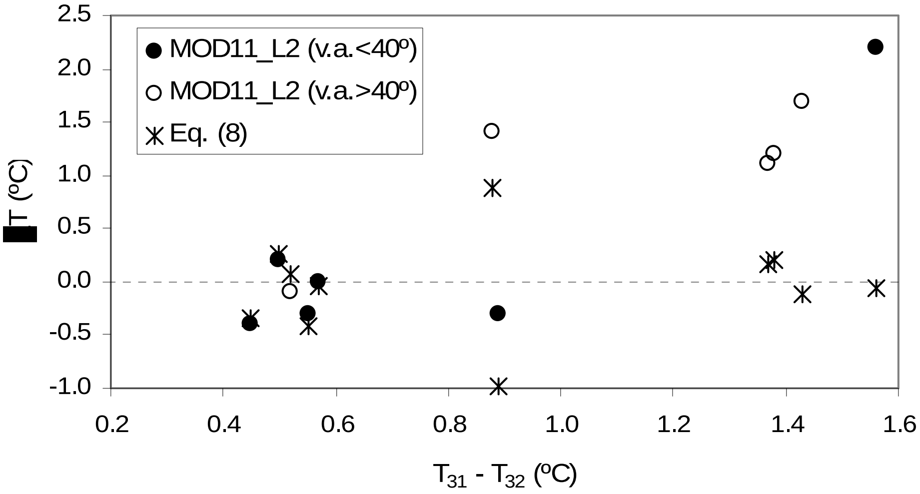

Figure 6. Temperature difference ΔT (ground minus algorithm LST) against the brightness temperature difference T_{31}-T_{32}, for the two MODIS LST algorithms (MOD11_L2 and Eq. 8). For MOD11_L2, cases with zenith viewing angle smaller than or larger than 40º are indicated.

TABLE CAPTIONS

Table 1. List of dates and time intervals with ground temperature measurements concurrent with Envisat/AATSR and Terra/MODIS overpasses.

Table 2. Ground LSTs (calibrated and emissivity corrected) and uncertainties measured concurrently with the AATSR overpass during the 2002 campaign.

Table 3. Ground LSTs (calibrated and emissivity corrected) and uncertainties measured concurrently with the MODIS overpass during the 2002-2004 campaigns.

Table 4. Brightness temperatures (in ºC) interpolated for the four pixels closest to the center of the test site, AATSR channels at 11 and 12 μm, nadir view. The standard deviation of temperatures, σ, and the satellite viewing angle, θ, are given.

Table 5. Brightness temperatures (in ºC) interpolated for the four pixels closest to the center of the test site, MODIS channels 31 and 32. The standard deviation of temperatures, σ, and the satellite viewing angle, θ, are given. The last column gives the atmospheric precipitable water, pw, obtained from the MODIS atmospheric profile product (MOD07).

Table 6. Comparison of ground and AATSR derived LSTs. The LST derived from the three algorithms is given as well as the difference between the ground and the algorithm LSTs.

Table 7. Comparison of ground and MODIS derived LSTs. The LST derived from the two algorithms is given as well as the difference between the ground and the algorithm LSTs. [a] Cirrus clouds. [b] θ>60º.

Table 1. List of dates and time intervals with ground temperature measurements concurrent with Envisat/AATSR and Terra/MODIS overpasses.

Year	**Date (day/month)**	**Ground measurements time (UTC)**	**Overpass time (UTC)**	
			AATSR	**MODIS**
2002	10/07	10:25 – 10:50	10:30	10:32
	13/07	10:30 – 11:00	10:37	–
	26/07	10:20 – 10:45	–	10:32
	29/07	10:25 – 10:53	10:34	–
	08/08	10:15 – 10:40	10:19	–
	14/08	10:20 – 10:45	10:31	–
2003	08/07	10:10 – 10:40	–	10:11
	11/07	10:13 – 10:45	–	10:42
	09/08	10:09 – 10:29	–	10:11
	12/08	10:19 – 10:36	–	10:42
	26/08	10:52 – 11:08	–	10:54
2004	08/07	10:14 – 10:30	–	10:24
	27/07	10:43 – 11:00	–	10:54
	03/08	10:46 – 11:10	–	11:00
	12/08	10:50 – 11:10	–	10:54

Table 2. Ground LSTs (calibrated and emissivity corrected) and uncertainties measured concurrently with the AATSR overpass during the 2002 campaign.

		Ground LST ± σ(T) (ºC)			
Date (day/month/year)	**AATSR overpass (UTC)**	**CE 1**	**Everest**	**AGA**	**average**
10/07/02	10:30	28.4±0.6	29.1±1.0	–	28.6±0.6
13/07/02	10:37	27.2±0.8	28.2±0.8	27.9±1.0	27.6±0.9
29/07/02	10:34	28.1±0.5	27.2±0.8	28.1±1.0	27.9±0.7
08/08/02	10:19	26.4±0.6	–	26.7±1.0	26.5±0.7
14/08/02	10:31	28.4±0.5	28.6±0.8	–	28.5±0.5

Table 3. Ground LSTs (calibrated and emissivity corrected) and uncertainties measured concurrently with the MODIS overpass during the 2002-2004 campaigns.

			Ground LST ± σ(T) (ºC)				
Year	**Date (day/month)**	**MODIS overpass (UTC)**	**CE 1**	**CE 2**	**Everest**	**AGA**	**average**
2002	10/07	10:32	28.6±0.5	–	29.6±0.9	–	28.8±0.7
	26/07	10:32	28.0±0.6	–	27.8±0.8	28.4±1.0	28.1±0.7
2003	08/07	10:11	28.6±0.4	28.6±0.4	29.1±0.9	–	28.7±0.5
	11/07	10:42	28.3±0.4	29.3±0.5	29.3±0.7	–	28.9±0.8
	09/08	10:11	30.1±0.6	29.1±0.7	–	29.7±0.7	29.7±0.8
	12/08	10:42	31.5±0.5	30.8±0.5	31.3±0.8	31.5±0.9	31.2±0.6
	26/08	10:54	31.5±0.4	32.2±0.5	–	–	31.9±0.6
2004	08/07	10:24	25.3±0.5	–	25.5±0.8	–	25.3±0.6
	27/07	10:54	27.9±0.6	27.8±0.5	–	–	27.9±0.6
	03/08	11:00	29.5±0.6	30.6±0.6	–	–	30.0±0.7
	12/08	10:54	28.6±0.5	28.8±0.3	–	–	28.7±0.5

Table 4. Brightness temperatures (in ºC) interpolated for the four pixels closest to the center of the test site, AATSR channels at 11 and 12 μm, nadir view. The standard deviation of temperatures, σ, and the satellite viewing angle, θ, are given.

Date (day/month/year)	**θ (º)**	**T_{11}**	**σ_{11}**	**T_{12}**	**σ_{12}**
10/07/02	3.7	25.07	0.03	23.03	0.02
13/07/02	13.8	22.25	0.05	19.22	0.04
29/07/02	8.8	22.90	0.05	21.03	0.05
08/08/02	16.2	20.29	0.07	17.31	0.07
14/08/02	3.9	23.77	0.06	21.58	0.03

Table 5. Brightness temperatures (in ºC) interpolated for the four pixels closest to the center of the test site, , MODIS channels 31 and 32. The standard deviation of temperatures, σ, and the satellite viewing angle, θ, are given. The last column gives the atmospheric precipitable water, pw, obtained from the MODIS atmospheric profile product (MOD07).

Date (day/month/year)	**θ (º)**	**T_{31}**	**σ_{31}**	**T_{32}**	**σ_{32}**	**pw (cm)**
10/07/02	43.7	23.89	0.15	23.01	0.16	2.42
26/07/02	43.7	21.68	0.06	20.25	0.06	2.88
08/07/03	60.3	22.22	0.02	20.84	0.04	2.22
11/07/03	27.7	26.68	0.18	26.23	0.17	1.60
09/08/03	60.5	23.30	0.32	21.93	0.21	2.21
12/08/03	28.1	28.23	0.10	27.73	0.08	1.47
26/08/03	6.7	24.73	0.05	23.17	0.04	2.99
08/07/04	50.3	22.46	0.62	21.94	0.65	1.90
27/07/04	5.6	25.45	0.06	24.90	0.06	1.68
03/08/04	6.1	26.92	0.13	26.03	0.15	2.68
12/08/04	5.7	25.81	0.03	25.24	0.04	2.03

Table 6. Comparison of ground and AATSR derived LSTs. The LST derived from the three algorithms is given as well as the difference between the ground and the algorithm LSTs.

Date (d/m/y)	**Ground LST (ºC)**	**AATSR LST (ºC)**			**Ground – AATSR LST (ºC)**		
		RAL proc.	**Eq. (4)**	**Eq. (7)**	**RAL proc.**	**Eq. (4)**	**Eq. (7)**
10/07/02	28.6	32.2	29.9	28.8	-3.6	-1.3	-0.2
13/07/02	27.6	31.8	29.6	28.3	-4.2	-2.0	-0.7
29/07/02	27.9	29.7	27.4	26.3	-1.8	0.5	1.6
08/08/02	26.5	29.4	27.6	26.2	-2.9	-1.1	0.3
14/08/02	28.5	30.9	29.0	27.8	-2.4	-0.5	0.7

bias (ºC)	-3.0	-0.9	0.3
standard deviation (ºC)	0.9	0.9	0.9

Table 7. Comparison of ground and MODIS derived LSTs. The LST derived from the two algorithms is given as well as the difference between the ground and the algorithm LSTs. † Cirrus clouds. * θ>40º. ** θ>60º.

Date (d/m/y)	**Ground LST (ºC)**	**MODIS LST (ºC)**		**Ground – MODIS LST (ºC)**	
		MOD11	**Eq. (8)**	**MOD11**	**Eq. (8)**
10/07/02*	28.8	27.4	27.9	1.4	0.9
26/07/02†,*	28.1	26.4	28.2	1.7	-0.1
08/07/03**	28.7	27.5	28.5	1.2	0.2
11/07/03	28.9	29.3	29.2	-0.4	-0.3
09/08/03**	29.7	28.6	29.5	1.1	0.2
12/08/03	31.2	31.0	30.9	0.2	0.3
26/08/03†	31.9	29.7	32.0	2.2	-0.1
08/07/04*	25.3	25.4	25.2	-0.1	0.1
27/07/04	27.9	28.2	28.3	-0.3	-0.4
03/08/04	30.0	30.3	31.0	-0.3	-1.0
12/08/04	28.7	28.7	28.7	0.0	0.0

bias (ºC)	0.6	0.0
standard deviation (ºC)	0.9	0.5